AGU PUBLICATIONS

JGR

Journal of Geophysical Research: Space Physics

RESEARCH ARTICLE

10.1002/2016JA023572

Key Points:
- Two groups of lower hybrid waves are observed in the ion diffusion and magnetospheric inflow regions
- In the magnetospheric inflow region lower hybrid waves develop when cold magnetospheric ions are present and can heat cold ions
- In the diffusion region lower hybrid waves develop at the density gradient and can cause cross-field particle diffusion

Correspondence to:
D. B. Graham,
dgraham@irfu.se

Citation:
Graham, D. B., et al. (2017), Lower hybrid waves in the ion diffusion and magnetospheric inflow regions, *J. Geophys. Res. Space Physics*, *122*, 517–533, doi:10.1002/2016JA023572.

Received 8 OCT 2016
Accepted 13 DEC 2016
Accepted article online 18 DEC 2016
Published online 21 JAN 2017

Lower hybrid waves in the ion diffusion and magnetospheric inflow regions

D. B. Graham[1], Yu. V. Khotyaintsev[1], C. Norgren[1,2], A. Vaivads[1], M. André[1], S. Toledo-Redondo[3], P.-A. Lindqvist[4], G. T. Marklund[4], R. E. Ergun[5], W. R. Paterson[6], D. J. Gershman[6,7], B. L. Giles[6], C. J. Pollock[6], J. C. Dorelli[6], L. A. Avanov[6,7], B. Lavraud[8,9], Y. Saito[10], W. Magnes[11], C. T. Russell[12], R. J. Strangeway[12], R. B. Torbert[13], and J. L. Burch[14]

[1]Swedish Institute of Space Physics, Uppsala, Sweden, [2]Department of Physics and Astronomy, Uppsala University, Uppsala, Sweden, [3]European Space Agency ESAC, Madrid, Spain, [4]Space and Plasma Physics, School of Electrical Engineering, KTH Royal Institute of Technology, Stockholm, Sweden, [5]Laboratory of Atmospheric and Space Physics, University of Colorado Boulder, Boulder, Colorado, USA, [6]NASA Goddard Space Flight Center, Greenbelt, Maryland, USA, [7]Department of Astronomy, University of Maryland, College Park, Maryland, USA, [8]Institut de Recherche en Astrophysique et Plantologie, Universit de Toulouse (UPS), Toulouse, France, [9]Centre National de la Recherche Scientifique, Toulouse, France, [10]Institute of Space and Astronautical Science, JAXA, Sagamihara, Japan, [11]Space Research Institute, Austrian Academy of Sciences, Graz, Austria, [12]Department of Earth and Space Sciences, University of California, Los Angeles, California, USA, [13]Space Science Center, University of New Hampshire, Durham, New Hampshire, USA, [14]Southwest Research Institute, San Antonio, Texas, USA

Abstract The role and properties of lower hybrid waves in the ion diffusion region and magnetospheric inflow region of asymmetric reconnection are investigated using the Magnetospheric Multiscale (MMS) mission. Two distinct groups of lower hybrid waves are observed in the ion diffusion region and magnetospheric inflow region, which have distinct properties and propagate in opposite directions along the magnetopause. One group develops near the ion edge in the magnetospheric inflow, where magnetosheath ions enter the magnetosphere through the finite gyroradius effect and are driven by the ion-ion cross-field instability due to the interaction between the magnetosheath ions and cold magnetospheric ions. This leads to heating of the cold magnetospheric ions. The second group develops at the sharpest density gradient, where the Hall electric field is observed and is driven by the lower hybrid drift instability. These drift waves produce cross-field particle diffusion, enabling magnetosheath electrons to enter the magnetospheric inflow region thereby broadening the density gradient in the ion diffusion region.

1. Introduction

Magnetic reconnection is a fundamental process in plasma physics, which transforms energy stored in magnetic fields into particle energy in the form of heating and acceleration [*Priest and Forbes*, 2000]. The most general form is asymmetric reconnection, in which the reconnecting plasmas on the two sides of the current sheet have different properties (e.g., density, temperature, and magnetic field strength) [*Swisdak et al.*, 2003; *Cassak and Shay*, 2007; *Pritchett*, 2008]. At Earth's magnetopause magnetic reconnection is generally asymmetric, where the dense magnetosheath plasma reconnects with the lower density magnetospheric plasma [*Paschmann et al.*, 1979; *Sonnerup et al.*, 1981]. Additionally, the magnetospheric plasma close to the equator is often composed of distinct hot and cold ion populations, as well as distinct hot and cold electron populations [*Chandler et al.*, 1999; *Sauvaud et al.*, 2001; *André and Cully*, 2012].

Asymmetric reconnection is known to differ significantly from symmetric reconnection, in which the reconnecting plasmas have the same properties. The Hall electric field tends to become monopolar, rather than dipolar, and the Hall magnetic field tends to become more dipolar rather than quadrupolar [*Cassak and Shay*, 2007; *Mozer et al.*, 2008]. In addition, the stagnation point is offset to the low-density side of the X line [*Cassak and Shay*, 2007], rather than being colocated with the X line. One of the characteristic features of asymmetric reconnection is intense parallel electron heating in the low-density inflow region [*Egedal et al.*, 2011], rather than in both inflow regions for symmetric reconnection [*Egedal et al.*, 2008; *Wang et al.*, 2010]. Simulations show that the parallel electron heating observed close to the ion diffusion region on the magnetospheric side is consistent with large-scale electric fields rather than heating by wave-particle interactions. Similar electron heating has been observed by Cluster [*Graham et al.*, 2014] and the Magnetospheric Multiscale (MMS) mission [*Graham et al.*, 2016a; *Khotyaintsev et al.*, 2016; *Lavraud et al.*, 2016].

Large-amplitude waves associated with magnetic reconnection are frequently observed. Often, the largest amplitude electric fields associated with magnetopause reconnection are due to lower hybrid drift waves [*Pritchett et al.*, 2012; *Graham et al.*, 2016a]. Lower hybrid drift waves often develop during magnetopause reconnection due to the sharp density gradients along the magnetospheric separatrix regions [*Krall and Liewer*, 1971; *Davidson and Gladd*, 1975; *Pritchett et al.*, 2012; *Pritchett*, 2013]. The role of lower hybrid waves in magnetic reconnection remains an outstanding question. Lower hybrid waves may play an important role in both symmetric and asymmetric reconnection by introducing particle diffusion [*Treumann et al.*, 1991; *Vaivads et al.*, 2004], anomalous resistivity [*Silin et al.*, 2005], and electron and ion heating [*Cairns and McMillan*, 2005]. Simulations of asymmetric reconnection show that electrostatic lower hybrid drift waves tend to form along the magnetospheric separatrix regions, rather than at the X line [*Pritchett et al.*, 2012; *Pritchett*, 2013; *Roytershteyn et al.*, 2012]. However, electromagnetic lower hybrid waves can develop within the current sheet close to the X line [*Daughton*, 2003; *Roytershteyn et al.*, 2012]. Previous estimates have shown that the anomalous resistivity and drag associated with the waves is small [*Bale et al.*, 2002; *Mozer et al.*, 2011], although a recent simulation of asymmetric reconnection showed that such effects may be significant near the diffusion region [*Price et al.*, 2016]. It is therefore important to characterize the properties of lower hybrid waves associated with magnetopause reconnection and determine what role they play.

In this paper we investigate the properties of the lower hybrid waves, which develop in the ion diffusion region and magnetospheric inflow region, and assess their effects on magnetic reconnection. The reconnection event we investigate is highly asymmetric, with a large density increase across the magnetopause. In the magnetosphere distinct hot and cold magnetospheric ions and electrons are present.

2. Observations

We use data from the Magnetospheric Multiscale (MMS) mission [*Burch et al.*, 2016]. MMS provides high-resolution fields and particle data enabling the structure of magnetic reconnection at electron and ion scales to be investigated in detail. We use data from electric field double probes (EDP) [*Lindqvist et al.*, 2016; *Ergun et al.*, 2016], fluxgate magnetometer (FGM) [*Russell et al.*, 2016], search coil magnetometer (SCM) [*Le Contel et al.*, 2016], and fast plasma investigation (FPI) [*Pollock et al.*, 2016]. We investigate the magnetopause crossing observed on 8 December 2015 between 00:05:50 UT and 00:06:20 UT. At this time the four spacecraft were in a tetrahedral configuration with inter-spacecraft separations of ~15 km. The spacecraft were located at [9.0, 3.9, 0.6] Earth radii in geocentric solar ecliptic (GSE) coordinates. We transform the vector data into LMN coordinates (unless otherwise stated), based on minimum variance analysis of the magnetic field **B** from MMS1 at the magnetopause crossing. The LMN coordinates are $\mathbf{L} = [0.25, -0.40, 0.88]$, $\mathbf{M} = [0.35, -0.89, 0.30]$ (dawnward), and $\mathbf{N} = [0.90, -0.23, -0.36]$ in GSE coordinates. The normal vector **N** is close to the minimum variance direction of the current density **J** computed using the Curlometer technique [*Dunlop et al.*, 1988]. From four-spacecraft timing of B_L at the current sheet we estimate the magnetopause boundary velocity to be $\mathbf{V}_{MP} \approx 80 \times [0.92, -0.16, -0.35]$ s^{-1} (GSE), which is closely aligned with **N**.

2.1. Overview

Figure 1 provides an overview of the magnetopause crossing from MMS1 (similar results are found by all four spacecraft). The spacecraft crosses the magnetopause from the magnetosheath into the magnetosphere. Based on the electron moments the ratio of magnetosheath to magnetospheric density is ~50. The magnetopause is characterized by a sharp reversal in B_L from southward to northward (Figure 1a). In the magnetosheath and magnetosphere B_M and B_N are both small, corresponding to a high-shear (negligible guide field) magnetopause crossing. A dipolar B_M is observed at the magnetopause crossing, consistent with the Hall magnetic field and is largest at the magnetopause crossing, where $B_L \approx 0$. Between 00:06:02 UT and 00:06:08 UT a northward ion ouflow region is observed, reaching ion speeds $V_i \sim 150$ km s^{-1} (Figure 1b). Based on the magnetospheric and magnetosheath conditions, we predict an outflow speed of ~ 400 km s^{-1} [*Cassak and Shay*, 2007], which is larger than the observed speed. This may indicate that the spacecraft cross the magnetopause close to the X line, where the outflow region has not fully developed. In the outflow region the ion motion becomes more field-aligned as seen in the ion pitch angle spectrogram in the spacecraft frame (Figure 1d).

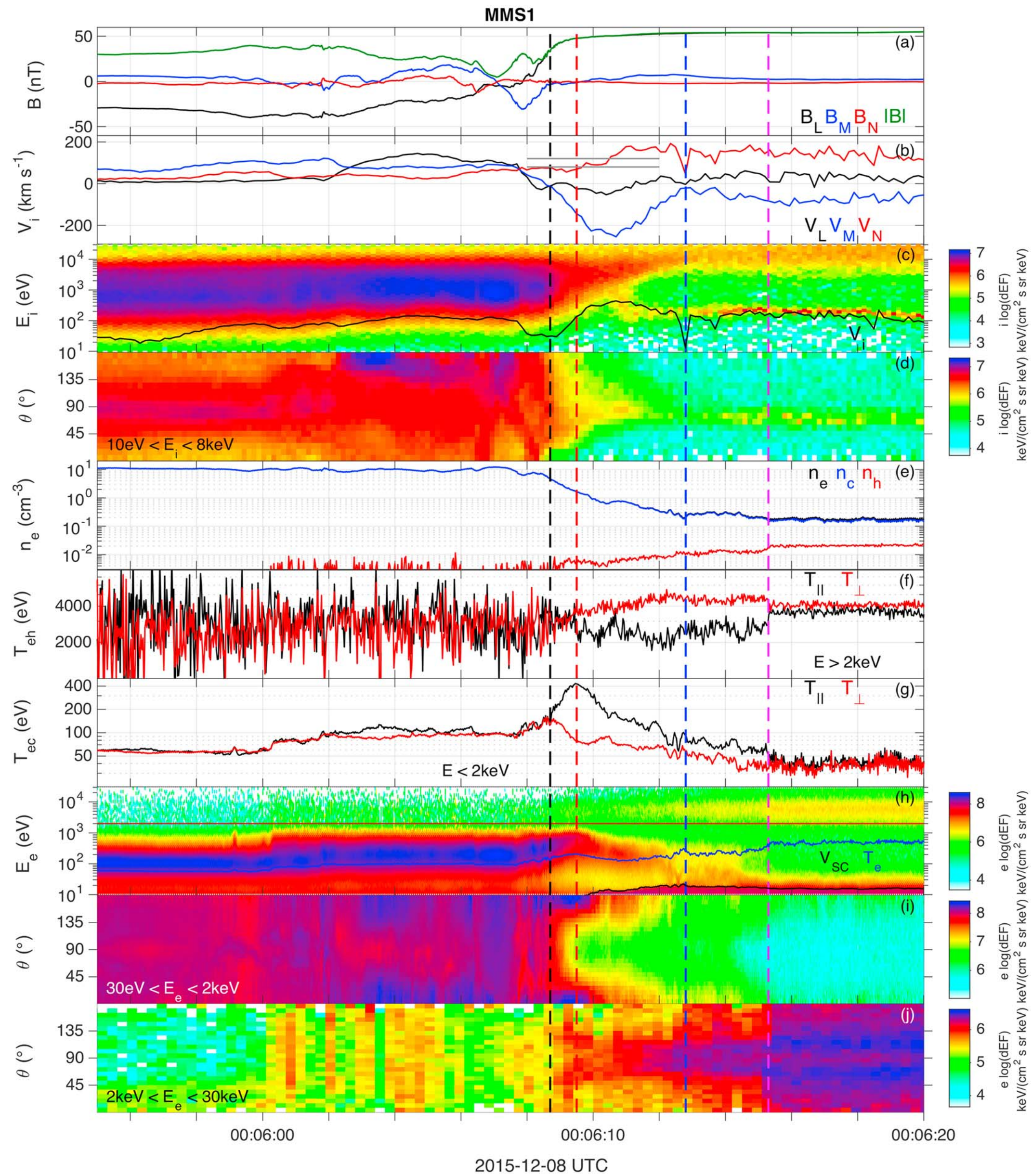

Figure 1. Overview of the magnetopause crossing observed by MMS1 on 8 December 2015. (a) **B**. (b) $\mathbf{V}_i$ (the grey lines indicate $V_{MP} = 80$ and 120 km s^{-1}). (c) Ion omnidirection differential energy flux (black line is energy associated with V_i). (d) Ion pitch angle distribution for energies 10 eV < E < 8 keV. (e) Electron densities of the total, cold, and hot populations n_e, n_c, and n_h, respectively. (f and g) $T_{\|}$ and $T_{\perp}$ of the hot and cold electron populations, respectively. (h) Electron omnidirection differential energy flux. The spacecraft potential V_{SC} and T_e are overplotted in black and blue, respectively. The red line marks the boundary between cold and hot electrons at 2 keV. (i and j) Electron pitch angle distributions for energies 30 eV < E < 2 keV and 2 keV < E < 30 keV, respectively. The black, red, blue, and magenta dashed lines indicate the diffusion region, peak parallel electron heating, ion edge, and electron edge, respectively.

In the outflow region the electron temperature T_e (Figures 1g and 1h) increases from $T_e \approx 60$ eV in the magnetosheath to $T_e \approx 100$ eV, indicating that the electrons are heated. On the magnetospheric side at ~00:06:11 UT, a large ion flow in the $-\mathbf{M}$ direction is observed. This flow is due to magnetosheath ions undergoing a partial gyroorbit into the magnetosphere. This can be seen in the omnidirectional ion differential energy flux, Figure 1c, where the highest-energy magnetosheath ions reach furthest into the magnetosphere. The furthest point reached by the magnetosheath ions into the magnetosphere is indicated by the blue dashed line in Figure 1, and termed the ion edge. Figure 1d shows that these ions have pitch angles θ centered around 90°, consistent with the spacecraft crossing the magnetopause close to the X line [*Khotyaintsev et al.*, 2016].

Further from the X line field-aligned ions are expected to be seen first by the spacecraft [*Khotyaintsev et al.*, 2006]. Figure 1c compares $V_{\mathrm{MP}} = 80$ km s^{-1} and $V_{\mathrm{MP}} = 120$ km s^{-1} (section 2.3), both indicated by gray lines, with the ion speed $V_{i\mathrm{N}}$ in the **N** direction. We see that $V_{iN} - V_{\mathrm{MP}}$ changes sign at ∼00:06:10 UT, which suggests that this is the location of the stagnation point. Therefore, the stagnation point occurs on the magnetospheric side of the X line, where B_L reverses direction, as expected for asymmetric magnetopause reconnection [*Cassak and Shay*, 2007].

We observe a cold magnetospheric ion population in the magnetosphere, seen as a narrow beam at $E \sim 200$ eV in Figure 1c after 00:06:12 UT. Based on partial moments of the magnetospheric ion distributions, we estimate that ∼80% of the ion density is contributed by these cold ions (not shown). As the cold ions approach the magnetopause, they are heated and accelerated in the region where the finite gyroradius effect in magnetosheath ions is observed. At 00:06:10.5 UT the cold ions have been heated and accelerated sufficiently so that they cannot be distinguished from the magnetosheath ions in Figures 1c and 1d.

In the magnetosphere we observe distinct cold and hot electron populations (Figure 1h), so we calculate the partial moments of these populations by dividing the electron distribution into hot (E>2 keV) and cold ($E < 2$ keV) populations. This cold electron population includes magnetosheath electrons and the cold magnetospheric population. Figure 1e shows the densities of the total, hot, and cold electron distributions, n_e, n_h, and n_c, respectively. In the magnetosphere the plasma is dominated by cold electrons, and the anisotropy in both hot and cold electrons is relatively small. From the magnetosphere to the magnetosheath n_h decreases and becomes negligible in the ion outflow and magnetosheath. Close to the magnetopause, temperature anisotropies develop between the boundaries marked by the black and magenta dashed lines in Figure 1. Within this region we observe $T_{\parallel} > T_{\perp}$ for the cold electron population and $T_{\parallel} < T_{\perp}$ for the hot population, Figures 1f and 1g, respectively, where $T_{\parallel}$ and $T_{\perp}$ are the parallel and perpendicular electron temperatures. The temperature anisotropy in the hot electrons is due to the decrease in electrons at pitch angles θ close to 0° and 180°, as seen in Figure 1j. The lack of loss-cone distributions at high energies suggests that MMS crosses the magnetopause close to the X line [*Graham et al.*, 2016b]. For the cold electrons the parallel temperature anisotropy is consistent with electron trapping observed in the inflow regions of asymmetric reconnection [*Egedal et al.*, 2011; *Graham et al.*, 2014, 2016a]. For cold electrons $T_{\parallel}$ peaks at ≈400 eV, well above the electron temperatures of the magnetosheath electrons and cold magnetospheric electrons. This parallel heating occurs in a region where magnetospheric and magnetosheath electrons are mixing. The maximum temperature anisotropy of cold electrons is $T_{\parallel c}/T_{\perp c} = 5.5$ and is observed on the magnetospheric side of the magnetopause (red dashed line in Figure 1). This peak occurs just before the stagnation point.

Based on the particle distributions and moments in Figures 1c–1j, we identify four boundaries (indicated by the dashed lines in Figure 1) on the magnetospheric side of the X line:

1. The black dashed line marks the center of the ion diffusion region. Since the spacecraft cross the magnetopause close to the X line this also indicates the magnetospheric separatrix, where E_N peaks (shown below). At this boundary parallel electron heating starts to develop. Around this time $T_{\perp}$ of the cold electrons is maximal. This boundary occurs also when $B_L > 0$ and marks when B_M becomes negligible, approximately the boundary between the magnetospheric **B** and when the Hall **B** starts to develop.
2. The red dashed line marks the peak in parallel electron heating, where $T_{\parallel}$ and $T_{\parallel}/T_{\perp}$ are maximal.
3. The blue dashed line marks the ion edge, the furthest point magnetosheath ions reach into the magnetosphere through the finite gyroradius effect.
4. The magenta dashed line is the electron edge, the boundary between unperturbed magnetosphere and the magnetospheric inflow region. This marks the boundary where hot magnetospheric electrons near $\theta = 0°$ and $\theta = 180°$ drop out, resulting in n_h decreasing and the $T_{\parallel}/T_{\perp} < 1$ anisotropy of hot electrons.

Based on the magnetopause speed $V_{\mathrm{MP}} \approx 80$ km s^{-1}, we estimate the distance between the center of the diffusion region and the electron edge to be 500 km $\approx 1 d_{i,\mathrm{MSP}} \approx 7 d_{i,\mathrm{MSH}}$, where $d_{i,\mathrm{MSP}} \approx 500$ km and $d_{i,\mathrm{MSH}} \approx 70$ km are the magnetospheric and magnetosheath ion inertial lengths. Similarly, we estimate the ion edge to be ∼300 km from the diffusion region, comparable to the gyroradius of the most energetic magnetosheath ions ($E_i \sim 10$ keV).

In summary, the magnetopause crossing is characterized by a reversal in B_L, northward ion outflow, Hall magnetic field, and large density asymmetry. We observe finite gyroradius magnetosheath ions entering the magnetosphere, very strong parallel electron heating, and the simultaneous loss in hot magnetospheric

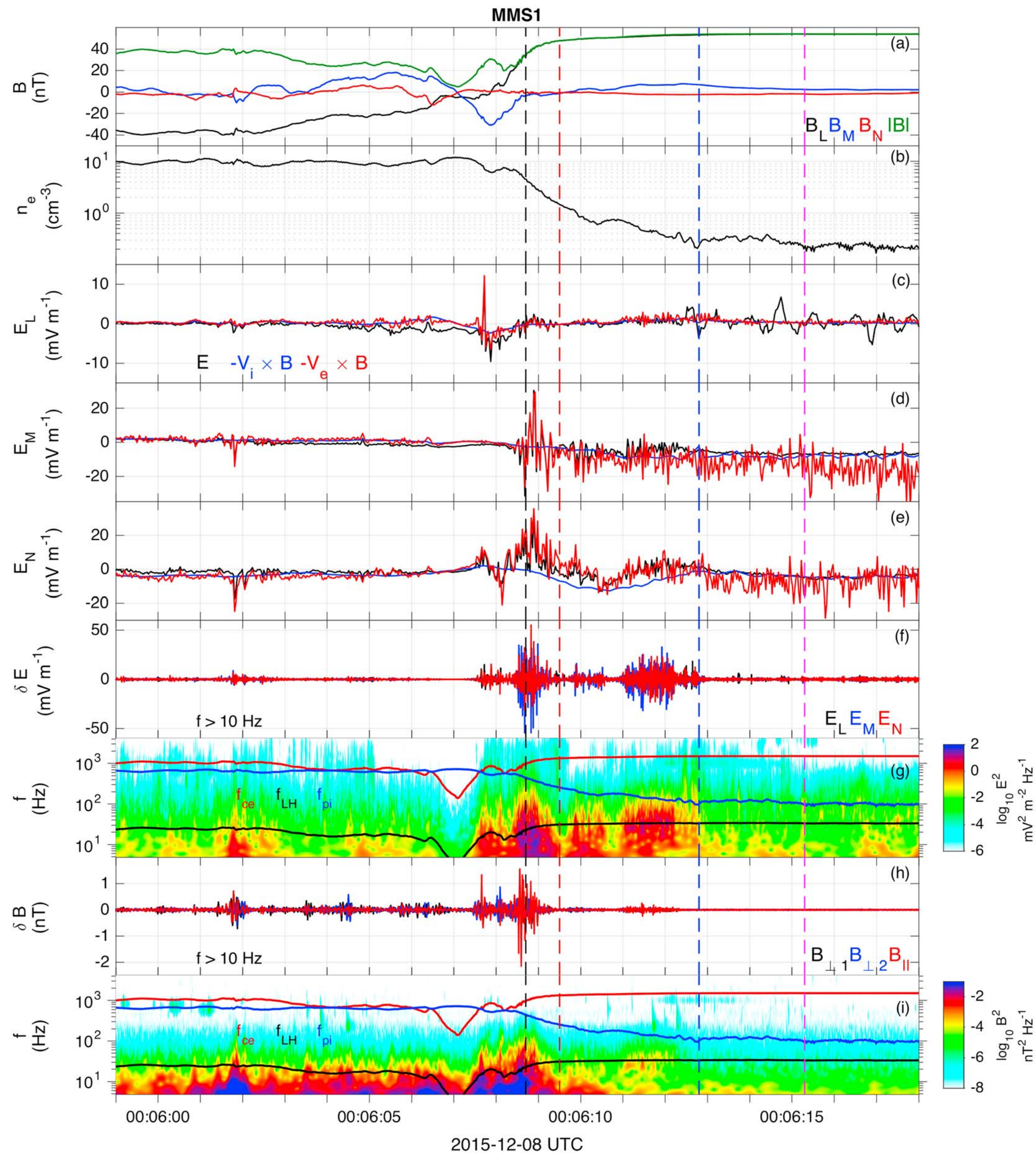

Figure 2. Electromagnetic fields observed by MMS1 at the magnetopause crossing. (a) **B**. (b) n_e. (c–e) **L**, **M**, and **N** components of **E** (black), $-\mathbf{V}_i \times \mathbf{B}$ (blue), and $-\mathbf{V}_e \times \mathbf{B}$ (red), respectively. (f) Fluctuating electric field $\delta\mathbf{E}$ with $f > 10$ Hz in LMN coordinates. (g) Spectrogram of **E**. (h) Fluctuating magnetic field $\delta\mathbf{B}$ with $f > 10$ Hz in field-aligned coordinates. (i) Spectrogram of **B**. The black, red, and blue lines in Figures 2g and 2i are f_{LH}, electron cyclotron frequency f_{ce}, and ion plasma frequency f_{pi}, respectively. The black, red, blue, and magenta dashed lines mark the diffusion region, peak parallel electron heating, ion edge, and electron edge, respectively.

electrons near $\theta = 0°$ and $\theta = 180°$ in the magnetospheric inflow region. The combination of these features is expected to be confined within $\sim 10\, d_{i,\mathrm{MSH}}$ from the X line [*Wang et al.*, 2016; *Phan et al.*, 2016]. We conclude that MMS crosses the magnetopause northward but close to the reconnection X line.

2.2. Fields and Waves

We now investigate the electromagnetic fields and waves associated with this reconnection event. We compare the ion convection $-\mathbf{V}_i \times \mathbf{B}$ term and electron convection $-\mathbf{V}_e \times \mathbf{B}$ term with the observed electric field **E** (resampled to the same frequency as the electron moments to remove high-frequency fluctuations). Figures 2c–2e show the **L**, **M**, and **N** components of **E**, $-\mathbf{V}_i \times \mathbf{B}$, and $-\mathbf{V}_e \times \mathbf{B}$, respectively. Throughout the magnetopause crossing the electrons remain frozen in to **B**, i.e., $\mathbf{E} \approx -\mathbf{V}_e \times \mathbf{B}$. However, the ions are not frozen in near the diffusion region, where $-\mathbf{V}_i \times \mathbf{B}$ is small. The normal electric field peaks at $E_N \sim 30$ mV m^{-1} near the diffusion region and is offset toward the X line from the peak parallel electron heating [*Graham et al.*, 2016a]. Between the diffusion region and the ion edge we observe a large $-\mathbf{V}_i \times \mathbf{B}$ in the $-\mathbf{N}$ direction, due to the flow of magnetosheath ions in the $-\mathbf{M}$ direction. This is the Larmor electric field found in simulations of asymmetric reconnection [*Malakit et al.*, 2013], and is expected to occur near the X line. Both $-\mathbf{V}_e \times \mathbf{B}$ and $\mathbf{E}$ are in the $-\mathbf{N}$ direction but are smaller than $-\mathbf{V}_i \times \mathbf{B}$.

Figure 2f shows the waveform of the fluctuating electric field $\delta\mathbf{E}$, with frequencies $f > 10$ Hz to remove fields that are not associated with wave activity. The largest amplitude $\delta\mathbf{E}$ are observed between the magnetopause crossing and the ion edge. The spectrogram of $\mathbf{E}$ (Figure 2g) shows that these fluctuations have frequencies close to the lower hybrid frequency $f_{\mathrm{LH}} \approx 30$–$40$ Hz, so we identify them as lower hybrid waves. We observe two distinct groups of waves located in the diffusion region and close to the ion edge. At the peak in parallel electron heating (red dashed line) negligible wave activity is observed. In the diffusion region the fluctuations are broadband, with maximum power just below the local f_{LH}. These fluctuating fields are observed at the same time as the density gradient and largest nonfluctuating electric field, suggesting that the lower hybrid drift instability is responsible for the waves. The waves near the ion edge are less broadband and centered around f_{LH}. Here the density gradient is much smaller. After the ion edge toward the magnetosphere no lower hybrid fluctuations are observed.

Increased magnetic field fluctuations $\delta\mathbf{B}$ ($f > 10$ Hz) are associated with the lower hybrid waves (Figure 2h). These fluctuations are primarily aligned with $\mathbf{B}$. The magnetic field fluctuations are substantially larger for the lower hybrid waves in the diffusion region, but $\delta\mathbf{B}$ are also observed for the lower hybrid waves near the ion edge. The $\delta\mathbf{B}$ fluctuations associated with lower hybrid waves are predicted to be primarily aligned with $\mathbf{B}$ [*Norgren et al.*, 2012], consistent with observations. Qualitatively, this can be understood as follows: assuming the electrons remain frozen in, while ions are demagnetized, the current density associated with the waves is $\mathbf{J} = -q_e n_e \delta\mathbf{E} \times \mathbf{B}/|\mathbf{B}|^2$. Therefore, $\mathbf{J}$ is significantly larger for the waves in the diffusion region than near the ion edge because of the increased n_e, which in turn produces larger $\delta\mathbf{B}$ according to Ampere's law.

Low-amplitude whistler emission is also observed in the inflow region, where $T_\parallel < T_\perp$ for the hot magnetospheric electrons, as well as in the magnetosheath (Figure 2i). The waves have frequencies $f_{\mathrm{ce}}/2 \lesssim f < f_{\mathrm{ce}}$, where f_{ce} is the electron cyclotron frequency. The likely source of the whistlers in the inflow region is the temperature anisotropy $T_\parallel / T_\perp < 1$ of the hot magnetospheric electrons.

To investigate the nature of the large-scale electric field in more detail, we compute the terms in the generalized Ohm's law:

$$\mathbf{E} + \mathbf{V}_i \times \mathbf{B} = \frac{\mathbf{J} \times \mathbf{B}}{q_e n_e} - \frac{\nabla \cdot \mathbf{P}_e}{q_e n_e}, \tag{1}$$

where q_e is the unit charge, $\mathbf{P}_e$ is the electron pressure tensor, and $\mathbf{J}$ is the current density calculated using the Curlometer technique [*Dunlop et al.*, 1988]. We compute $\nabla \cdot \mathbf{P}_e$ from the differences in the full pressure tensor measured by each spacecraft. We average $\mathbf{E}$ and the convection terms over the four spacecraft. Figures 3a and 3b show the four-spacecraft average of $\mathbf{B}$ and $\mathbf{J}$. Large $\mathbf{J}$ is observed at the magnetopause in the $\mathbf{L}$ and $-\mathbf{M}$ directions. Figure 3c shows the four-spacecraft average of $\mathbf{E}$, which is very similar to Figure 2e.

In Figure 3d we plot the $\mathbf{N}$ components of the terms in equation (1). Throughout the magnetopause crossing the electrons are approximately frozen in; i.e., $\mathbf{E} \approx -\mathbf{V}_e \times \mathbf{B}$. In the diffusion region the Hall term $\mathbf{J} \times \mathbf{B}/q_e n_e$, $-\mathbf{V}_e \times \mathbf{B}$ and $\mathbf{E}$ are large, whereas $-\mathbf{V}_i \times \mathbf{B}$ is negligible. However, $-\mathbf{V}_i \times \mathbf{B}$ is significantly larger than $-\mathbf{V}_e \times \mathbf{B}$ and $\mathbf{E}$ in the $-\mathbf{N}$ direction between the region of intense electron heating and the ion edge. As a result, $\mathbf{J} \times \mathbf{B}/q_e n_e$ remains positive, corresponding to a small cross-field current. Throughout the interval the electron pressure term $-\nabla \cdot \mathbf{P}_e / q_e n_e$ remains small compared with the other terms (peaking at -3.5 mV m^{-1} in the $\mathbf{N}$ direction) and has the opposite sign to the Hall term [*Henderson et al.*, 2006]. Figure 3e shows the $\mathbf{N}$ components of the left-hand side and right-hand side of equation (1). We find good agreement between these terms, indicating that equation (1) remains valid for this reconnection event, and $\mathbf{E} + \mathbf{V}_i \times \mathbf{B}$ is approximately balanced by $\mathbf{J} \times \mathbf{B}/q_e n_e$.

The structure of the ion diffusion region and magnetospheric inflow region is shown in Figure 4, along with the spacecraft trajectory through the reconnection event. In brief, on the magnetospheric side of the X line two spatially separated groups of lower hybrid waves are observed. The peak in the parallel electron heating occurs between the two groups of waves. These observations show that the diffusion region and magnetospheric inflow region have a complicated structure.

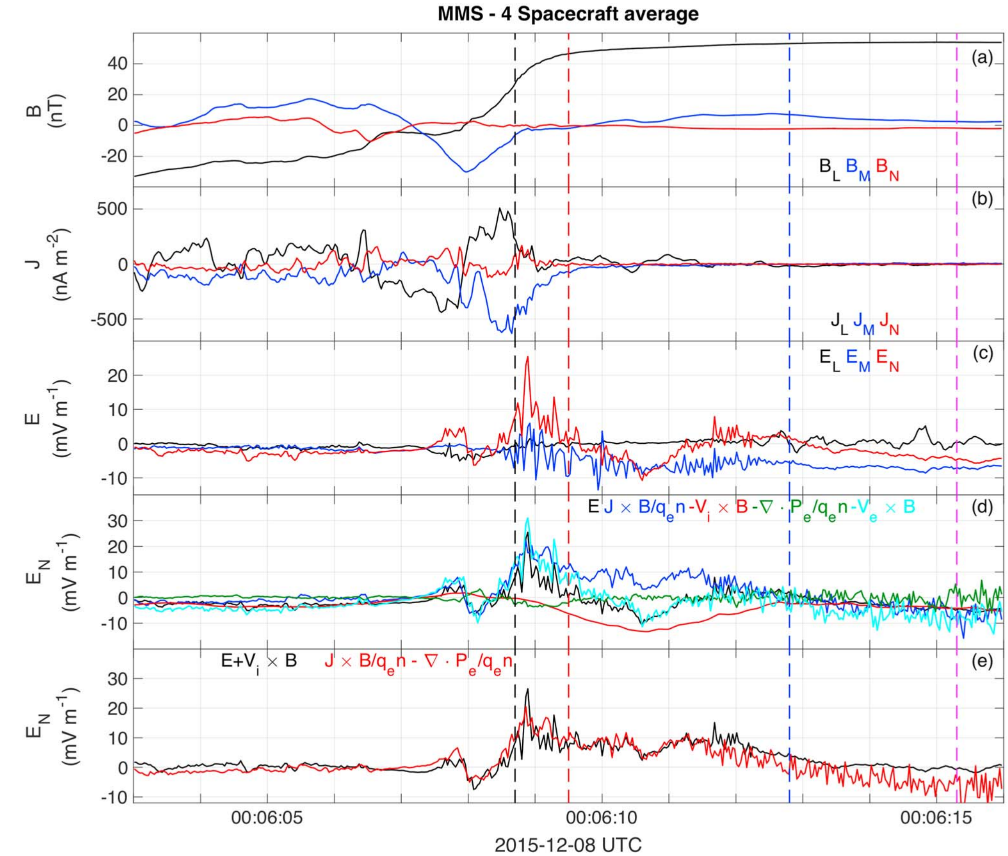

Figure 3. Electric field, current density, and the terms in the generalized Ohm's law based on four-spacecraft observations. All quantities correspond to four-spacecraft averages. (a) **B**. (b) **J** calculated using the Curlometer technique. (c) **E**. (d) Normal components of **E** (black), $\mathbf{J} \times \mathbf{B}/q_e n_e$ (blue), $-\mathbf{V}_i \times \mathbf{B}$ (red), $-\nabla \cdot \mathbf{P}/q_e n_e$ (green), and $-\mathbf{V}_e \times \mathbf{B}$ (light blue). (e) Normal components of $\mathbf{E} + \mathbf{V}_i \times \mathbf{B}$ (black) and $\mathbf{J} \times \mathbf{B}/q_e n_e - \nabla \cdot \mathbf{P}/q_e n_e$ (red). The black, red, blue, and magenta dashed lines mark the diffusion region, peak parallel electron heating, ion edge, and electron edge, respectively.

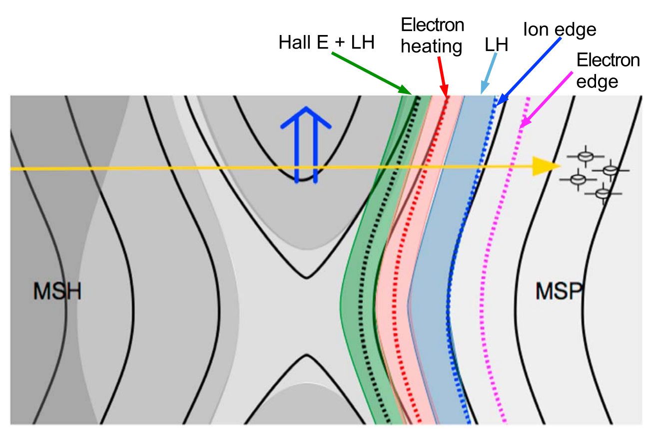

Figure 4. Sketch of MMS trajectory through the 8 December 2015 reconnection region. The magnetospheric inflow is characterized by intense parallel electron heating (red shaded region) and two distinct spatially separated groups of lower hybrid waves (green and blue shaded regions). Parallel electron heating is observed between the two groups of lower hybrid waves. The black, red, blue, and magenta dashed lines indicate the diffusion region, peak parallel electron heating, ion edge, and electron edge, respectively.

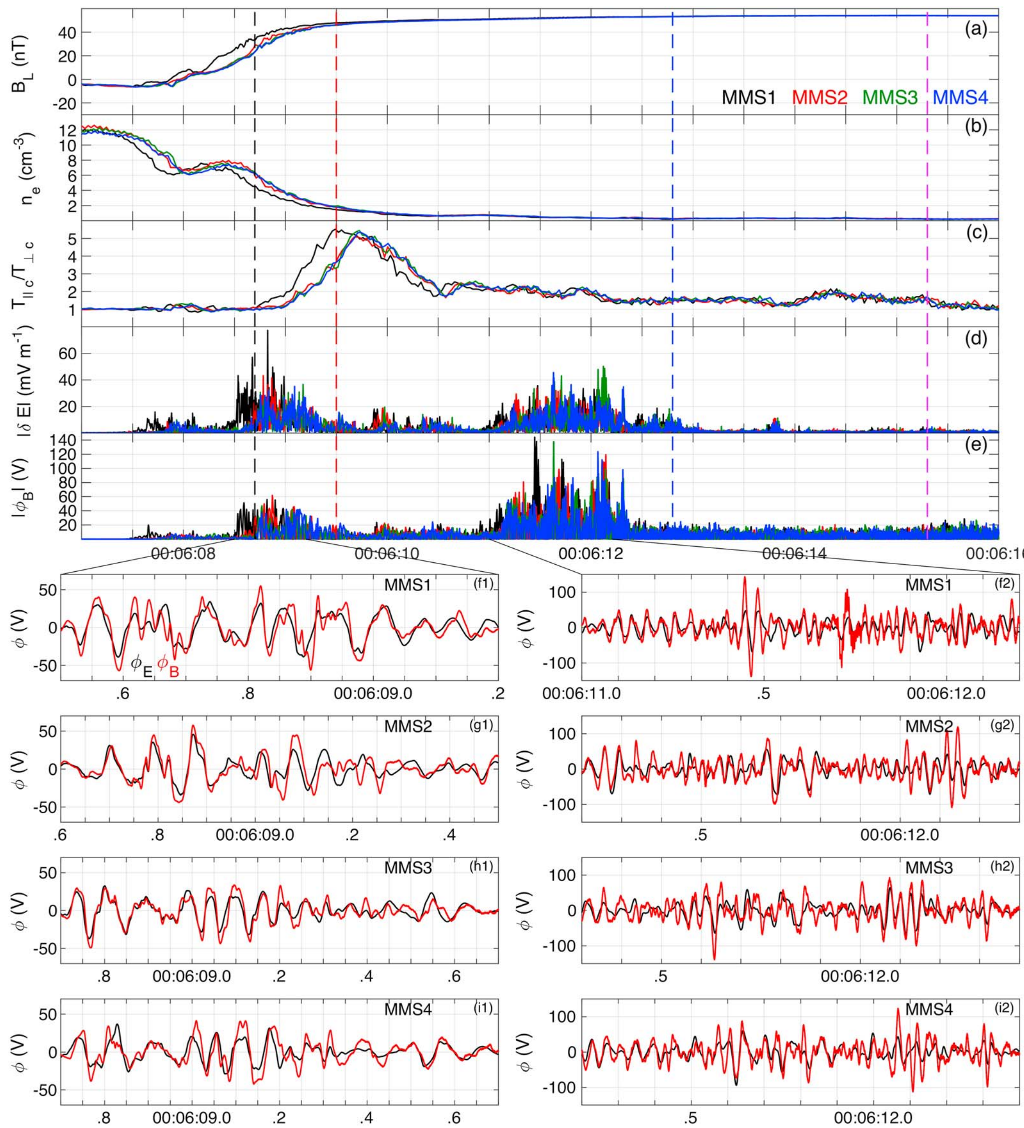

Figure 5. Properties of the lower hybrid waves observed by the four MMS spacecraft. (a – e) B_L, n_e, $T_{\|c}/T_{\perp c}$, $|\delta \mathbf{E}|$, and ϕ_B from MMS1–MMS4, respectively. The black, red, blue, and magenta dashed lines mark the diffusion region, peak parallel electron heating, ion edge, and electron edge, respectively (obtained from MMS1). (f–i) ϕ_E and ϕ_B of the lower hybrid waves observed by MMS1–MMS4, respectively.

2.3. Lower Hybrid Wave Observations

In this section we investigate the properties of the lower hybrid waves observed in the diffusion and inflow regions. Figures 5a–5c show B_L, n_e, and $T_{\|c}/T_{\perp c}$ from each spacecraft, respectively. MMS1 crosses the magnetopause before the other spacecraft, which cross the magnetopause at similar times. The profiles of B_L, n_e, and $T_{\|c}/T_{\perp c}$ are similar on each spacecraft. The changes in $T_{\|c}/T_{\perp c}$ are approximately the same on each spacecraft except for the offsets in time, indicating a spatial structure, which should move with the magnetopause [*Graham et al.*, 2016a]. Using these time offsets, we can estimate the speed of the structure. From time differences in $T_{\|c}/T_{\perp c}$ on the magnetopause (left) side of the peak in $T_{\|c}/T_{\perp c}$ we estimate $V_N \approx 80$ km s^{-1}, consistent with the estimated magnetopause boundary speed. On the magnetospheric inflow (right) side of the peak $T_{\|c}/T_{\perp c}$ we estimate $V_N \approx 120$ km s^{-1}. This suggests that the magnetopause boundary may be accelerating outward, as the spacecraft cross the magnetopause, or that the region of electron heating is contracting.

The magnitudes of $\delta\mathbf{E}$ ($f > 10$ Hz) associated with the lower hybrid waves are shown in Figure 5d for each spacecraft. All spacecraft observe the two distinct groups of lower hybrid waves. The amplitudes of the waves are comparable on each spacecraft. By comparing Figures 5c and 5d, we see that the lower hybrid waves

Table 1. Properties of the Lower Hybrid Waves Observed in the Diffusion Region and Near the Ion Edge[a]

	Diffusion Region Waves				Ion Edge Waves			
MMS	v (km s^{-1})	Direction (LMN)	λ (km)	C_ϕ	v (km s^{-1})	Direction (LMN)	λ (km)	C_ϕ
1	148	[0.07,0.88,–0.48]	10	0.82	362	[0.13,–0.94,0.32]	12	0.62
2	174	[0.08,0.96,0.27]	12	0.78	394	[0.13,–0.99,0.06]	13	0.69
3	194	[0.07,0.95,0.31]	13	0.85	314	[0.12,–0.99,0.02]	10	0.67
4	155	[0.07,0.98,–0.20]	10	0.75	323	[0.12,–0.99,-0.12]	11	0.64

[a]The properties are calculated for electric and magnetic field fluctuations above 10 Hz.

develop on both sides of the peak in $T_{\|c}/T_{\perp c}$, and very little $|\delta\mathbf{E}|$ is observed when $T_{\|c}/T_{\perp c}$ peaks. The lack of intense lower hybrid waves near the peak in $T_{\|c}/T_{\perp c}$ is consistent with *Graham et al.* [2016a] and suggests that the lower hybrid waves are not directly involved in the parallel electron heating.

The wave potential ϕ_B of the lower hybrid waves can be calculated from $\delta B_\|$ and the local plasma conditions [*Norgren et al.*, 2012], using

$$\phi_B = \frac{|\mathbf{B}|}{q_e n_e \mu_0}\delta B_\| . \tag{2}$$

Figure 5e shows $|\phi_B|$ computed for each spacecraft from $\delta B_\|$ bandpassed above 10 Hz. The largest fluctuations in $|\phi_B|$ correspond to the largest $|\delta\mathbf{E}|$. We find that $|\phi_B|$ peaks at ∼60 V and ∼ 140 V for the lower hybrid waves in the diffusion region and near the ion edge, respectively. The peak $|\phi_B|$ correspond to $\phi_B/T_e \sim 0.4$ and $\phi_B/T_e \sim 0.9$, respectively, where the total electron temperature is used. When the cold electron temperature T_{ec} is used, we calculate $\phi_B/T_{ec} \sim 1.7$ for the lower hybrid waves near the ion edge. Such large wave potentials could indicate that the waves are in the nonlinear regime and are likely an important source of particle scattering.

To calculate the phase velocity $\mathbf{v}_{ph}$ of the lower hybrid waves, we fit the potential calculated by integrating $\delta\mathbf{E}$ (for $f > 10$ Hz), $\phi_E = \int \delta\mathbf{E}dt \cdot \mathbf{v}_{ph}$. The phase speed v_{ph} and propagation direction are found by finding the best fit of ϕ_E to ϕ_B, where $\mathbf{v}_{ph}$ is a free parameter [*Norgren et al.*, 2012; *Graham et al.*, 2016a; *Khotyaintsev et al.*, 2016; *Innocenti et al.*, 2016]. Figures 5f–5i show ϕ_B and the best fit of ϕ_E to ϕ_B for the lower hybrid waves observed by each spacecraft in the diffusion region and near the ion edge. In each case we find good fits of ϕ_E to ϕ_B over the regions of largest $\delta\mathbf{E}$ and ϕ_B fluctuations. This indicates that the estimated $\mathbf{v}_{ph}$ are reliable. The properties of the lower hybrid waves are summarized in Table 1. For both groups of lower hybrid waves there is good agreement between the four spacecraft, meaning there is little change in the wave properties over the spacecraft separations of ∼15 km. The primary difference is that slightly different directions are found on MMS1, which crosses the magnetopause slightly earlier than the other spacecraft.

The lower hybrid waves observed in the diffusion region propagate approximately in the **M** direction (dawnward) along the magnetopause. The wavelength λ is calculated using $\lambda = v_{ph}/f$, where $f \sim 15$ Hz is the wave frequency around where the power peaks. We calculate 10 km $\lesssim \lambda \lesssim$ 13 km, which corresponds to wave numbers $k\rho_e \approx 0.4$–1.0, where $\rho_e = m_e v_{\perp e}/(q_e B)$ is the thermal electron gyroradius and $v_{\perp e}$ is the perpendicular electron thermal speed. This range of $k\rho_e$ is consistent with the electrostatic lower hybrid drift wave. By averaging the large-scale **E** over the time the lower hybrid waves are observed, we estimate the $\mathbf{E}\times\mathbf{B}$ velocity $\mathbf{V}_E = \mathbf{E}\times\mathbf{B}/|\mathbf{B}|^2$ to be $\mathbf{V}_E \approx 180 \times [0.10, 0.91, 0.41]$ km s^{-1} (LMN). Therefore, the observed lower hybrid waves propagate at approximately the electron convection velocity $\mathbf{V}_E$, consistent with previous observations [*Norgren et al.*, 2012]. We note that the pressure gradient is in the **N** direction and **B** is along the **L** direction, so the electron diamagnetic drift is approximately in the **M** direction. Therefore, these lower hybrid drift waves propagate in the electron diamagnetic drift direction, rather than the ion diamagnetic drift direction. These wave properties are consistent with electrostatic lower hybrid drift waves produced at the density gradient in the magnetospheric separatrices of asymmetric reconnection [*Pritchett et al.*, 2012; *Roytershteyn et al.*, 2012; *Pritchett*, 2013].

The lower hybrid waves observed near the ion edge have distinct properties to the waves in the diffusion region. In particular, the waves propagate in the −**M** direction (duskward) and have significantly larger v_{ph}. To estimate λ, we assume $f \sim 30$ Hz, which corresponds to the maximum power. Based on this assumption,

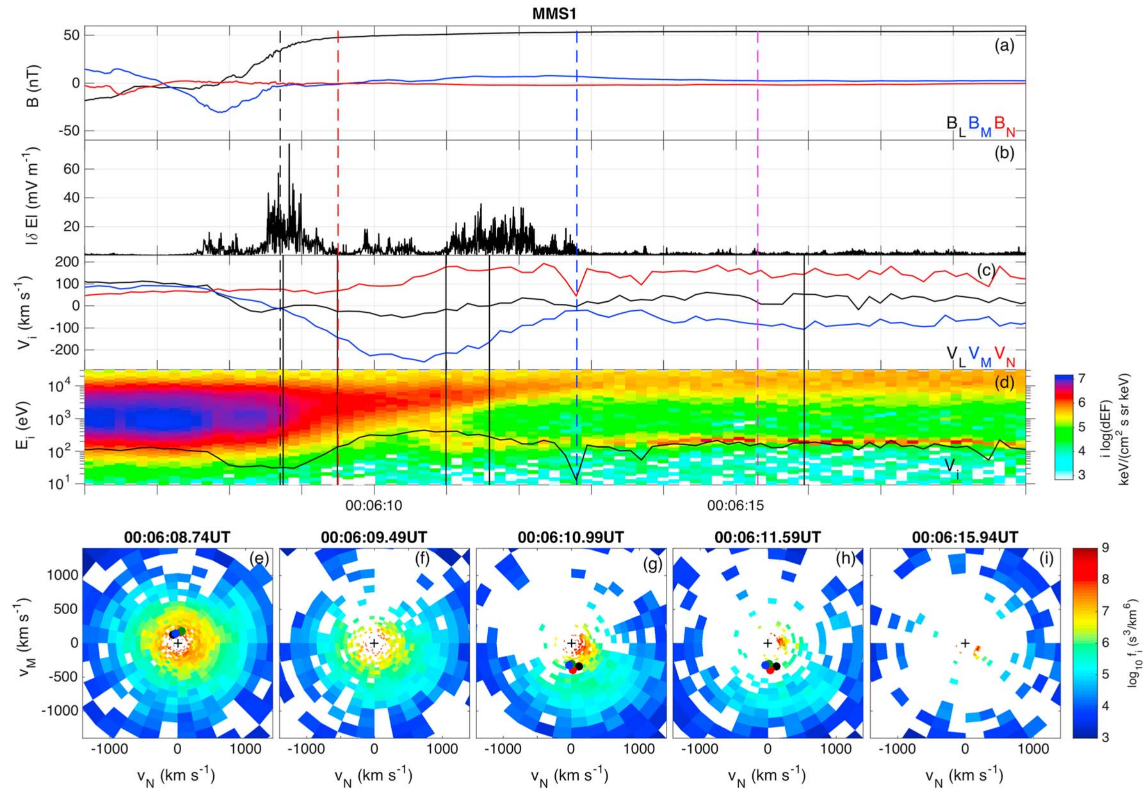

Figure 6. Ion distributions in the diffusion region and magnetospheric inflow region observed by MMS1. (a–d) **B**, $|\delta \mathbf{E}|$, $\mathbf{V}_i$, and omnidirection ion differential energy flux (black line is the energy of V_i). The black, red, blue, and magenta dashed lines in Figures 6a–6d mark the diffusion region, peak parallel electron heating, ion edge, and electron edge, respectively. (e–i) Ion distributions in the **M**-**N** plane from the diffusion region and inflow region. From left to right the distributions correspond to the times indicated by the black vertical lines in Figures 6c and 6d. The black, red, green, and blue circles in Figures 6d, 6f, and 6g correspond to the lower hybrid wave phase velocities observed by MMS1–MMS4, respectively.

these waves have wavelengths 10 km $\lesssim \lambda \lesssim$ 13 km, comparable to the waves in the diffusion region. Based on the local ρ_e, we estimate $k\rho_e \approx 0.3$–0.6, somewhat smaller than the estimates in the diffusion region, but consistent with electrostatic lower hybrid waves. When these waves are observed the average $\mathbf{V}_E$ is $120 \times [0.02, 0.11, 0.99]$ km s^{-1} (LMN), so in this case the waves propagate neither in the $\mathbf{V}_E$ direction nor at a similar speed, in contrast to the lower hybrid waves in the diffusion region. We conclude that the observed waves are consistent with lower hybrid waves, although the properties differ from the waves observed in the diffusion region.

2.4. Ion Behavior in the Inflow Region

In this section we investigate the behavior of the magnetosheath and cold magnetospheric ions in the magnetospheric inflow region and their relation to the lower hybrid waves. Figures 6a–6d provide an overview from MMS1 of the diffusion region and magnetospheric inflow region showing **B**, $|\delta \mathbf{E}|$, $\mathbf{V}_i$, and the omnidirection ion differential energy flux, respectively. From Figure 6d we can observe the behavior of the cold ions as they enter the diffusion region. In the magnetosphere the cold ions have very low temperatures $T_i \sim 20$ eV (comparable to the energy channel width). There is little change in the cold ion behavior as they cross the electron edge, but they are heated as they cross the ion edge [*Toledo-Redondo et al.*, 2016]. Around 00:06:11 UT this heating is clearly observed, and at this point the cold ions are also accelerated so that at ∼ 00:06:10.5 UT (around the stagnation point) and closer to the magnetopause they are indistinguishable from the magnetosheath ions.

To investigate the dynamics of the ions in more detail, we plot two-dimensional cuts of the three-dimensional ion distributions in the **M**-**N** plane. Figures 6e–6i show five ion distributions at the times indicated by the black vertical lines in Figures 6c and 6d. In the ion diffusion region (Figure 6e) the ions are nearly isotropic and have a small drift in the **N** direction. Further into the magnetosphere, the magnetosheath ions are characterized by a crescent-shaped distribution centered along the −**M** direction (Figures 6f–6h). This crescent corresponds to the magnetosheath ions undergoing a partial gyroorbit into the magnetosphere [*Wang et al.*, 2016;

Phan et al., 2016]. When the peak in electron parallel heating is observed, the crescent covers a wide range of speeds and angles (Figure 6f) and no trace of the cold ions is observed, indicating that they have been heated and accelerated by the time they reach this point. Therefore, the cold magnetospheric ions likely have no effect on the parallel electron heating and the processes operating in the diffusion region. Closer to the ion edge, the crescent becomes narrower in speed because only the highest-energy magnetosheath ions, with the largest gyroradius, reach these points. Similarly, the angular width and density of the crescent decrease toward the ion edge, after which magnetosheath ions are no longer observed. However, the temperature of the crescent, computed from the distribution function excluding cold ions, tends to increase toward the ion edge (not shown).

In the magnetosphere (Figure 6i) the cold ions are seen as a very narrow beam closely aligned with the **N** direction, with a speed of $V_{\rm ic} \approx 150$ km s^{-1} in the spacecraft frame. Based on timing analyses of $T_{\parallel c}/T_{\perp c}$ in the inflow region (section 2.3) the ion inflow speed is ~30 km s^{-1}, which is reasonable for magnetopause reconnection. (Note that for $V_{\rm MP} = 80$ km s^{-1} the inflow speed is ~70 km s^{-1}, which is quite large for magnetopause reconnection.) In Figure 6h the cold ions have crossed the ion edge and still propagate along the **N** direction but have been heated slightly; the cold ions broaden in angle and speed. Further heating is observed in Figure 6g, and the cold ion bulk velocity has increased in the −**M** direction, reducing the relative speed of the crescent to the cold ions. Thus, the region of cold ion heating is colocated with the lower hybrid waves near the ion edge. The cold ions are accelerated in the −**M** direction by the Larmor electric field set up by the finite gyroradius magnetosheath ions. The cold ions behave like pickup ions and become indistinguishable from the magnetosheath ions.

In Figures 6e, 6g, and 6h the colored circles indicated the phase velocities of the lower hybrid waves (diffusion region lower hybrid waves in Figure 6e and ion edge lower hybrid waves in Figures 6g and 6h). In the ion diffusion region the ion distribution shows no features suggestive of an unstable distribution; however, since the ion distribution has negligible V_M and the electrons are drifting in the **M** direction, the likely source of the instability is the relative electron and ion drifts.

The ion distributions where the ion edge lower hybrid waves are observed show evidence of instability. In this region the cold magnetospheric ions and the crescent distribution of magnetosheath ions are distinct from each other. The relative drift between the two ion populations in the **M** direction perpendicular to **B** can excite the ion-ion cross-field instability, which produces lower hybrid-like waves [*Papadopoulos et al.*, 1971; *Gary et al.*, 1987]. The observed waves have phase velocities approximately between the two ion populations, consistent with an instability developing between the two ion populations producing the waves. When only cold magnetospheric ions are observed in the magnetosphere or when the cold magnetospheric ions become indistinguishable from the magnetosheath ions near the stagnation point, there is negligible lower hybrid wave activity. Therefore, the ion-ion cross-field instability associated with the distinct ion populations is the likely source of the lower hybrid waves observed near the ion edge, as described in section 2.5.2.

2.5. Lower Hybrid Instability Analysis

2.5.1. Lower Hybrid Drift Instability

We now investigate in detail the instabilities producing the lower hybrid waves by solving the relevant dispersion equations using the local plasma conditions. For the lower hybrid waves in the diffusion region at the density gradient we assume the lower hybrid waves propagate perpendicular to both **B** and the density gradient, i.e., the **M** direction. The relevant local electrostatic dispersion equation is [*Krall and Liewer*, 1971; *Davidson and Gladd*, 1975]

$$0 = 1 - \frac{\omega_{\rm pi}^2}{k^2 v_i^2} Z'\left(\frac{\omega}{k v_i}\right) + \frac{\omega_{\rm pe}^2}{\Omega_{\rm ce}^2}\frac{1 - I_0(b)\exp(-b)}{b} + \frac{2\omega_{\rm pe}^2}{k^2 v_e^2}\frac{k V_\Delta(k)}{\omega - k V_E}, \tag{3}$$

where $\omega_{pi,e} = \sqrt{n_{i,e} q_e^2 / m_{i,e} \epsilon_0}$ are the ion and electron plasma frequencies, $v_{i,e}$ are the ion and electron thermal speeds, $b = k^2 v_e^2 / 2\Omega_{\rm ce}^2$, $\Omega_{\rm ce}$ is the electron cyclotron frequency, Z' is the derivative of the plasma dispersion function, I_0 is the modified Bessel function of first kind of order zero, and $V_\Delta(k)$ is defined as

$$V_\Delta(k) = \frac{v_e^2}{2\Omega_{\rm ce}} I_0(b)\exp(-b)\frac{1}{n_e}\frac{\partial n_e}{\partial x}. \tag{4}$$

For equation (4) the terms associated with $\partial B/\partial x$ and $\partial T_e/\partial x$ are neglected because their effects are small compared with $\partial n_e/\partial x$. Here k is assumed to be along the **M** direction. In equation (3) the ion distribution is

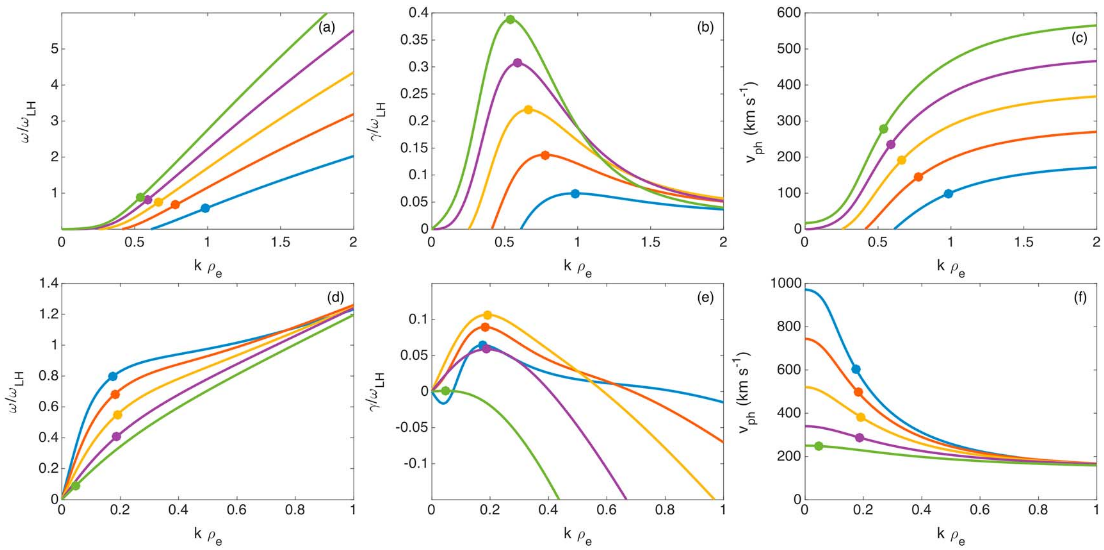

Figure 7. Properties of the lower hybrid waves in the diffusion region and near the ion edge. (a) Dispersion relations, (b) growth rates, and (c) phase speeds predicted by equation (3) for $V_E = 200$ km s^{-1} (blue), 300 km s^{-1} (red), 400 km s^{-1} (yellow), 500 km s^{-1} (purple), and 600 km s^{-1} (green). The other parameters are stated in the text. (d) Dispersion relations, (e) growth rates, and (f) phase speeds predicted by equation (5). The blue, red, orange, purple, and green curves correspond to cases 1–5 defined in the text, respectively. The circles indicate the points corresponding to the maximum growth rate.

assumed to be stationary, which is justified based on Figure 6e. We use the plasma conditions $n_e = 4$ cm^{-3}, $T_e = 150$ eV, $T_i = 1$ keV, $B = 40$ nT, and $n_e^{-1}\partial n_e/\partial x = 2\times10^{-5}$ m^{-1}, based on the observed plasma conditions. Based on Figure 2e the mean V_E in the diffusion region is ∼200 km s^{-1}, while the maximum V_E is ≈ 700 km s^{-1}. We therefore consider five cases for $V_E = 200$ km s^{-1}, 300 km s^{-1}, 400 km s^{-1}, 500 km s^{-1}, and 600 km s^{-1} (cases 1–5, respectively).

The dispersion relations, growth rates γ, and $v_{\rm ph}$ as functions of k obtained from equation (3) are shown in Figures 7a–7c, respectively. All five cases exhibit positive growth. As V_E increases ω, γ, and $v_{\rm ph}$ increase. The wave numbers $k_{\rm max}$ corresponding to maximum growth rate $\gamma_{\rm max}$ are $0.5 \lesssim k_{\rm max}\rho_e \lesssim 1$ for the five cases and $k_{\rm max}\rho_e$ decreases as V_E increases. This corresponds to wavelengths 7 km $\lesssim \lambda \lesssim$ 12 km, in good agreement with the estimates in Table 1. The corresponding range of frequencies is $0.6 \lesssim \omega/\omega_{\rm LH} \lesssim 0.9$, or equivalently, 15 Hz $\lesssim f \lesssim$ 25 Hz, in good agreement with the power spectrum in Figure 2g. The range of $v_{\rm ph}$ corresponding to $\gamma_{\rm max}$ is 100 km s$^{-1} \lesssim v_{\rm ph} \lesssim$ 300 km s^{-1} for the five cases. For cases 2 ($V_E = 300$ km s^{-1}) and 3 ($V_E = 400$ km s^{-1}) we predict $v_{\rm ph} = 150$ km s^{-1} and $v_{\rm ph} = 190$ km s^{-1}, respectively, in excellent agreement with observations (Table 1). In conclusion, the waves observed in the ion diffusion region are well explained by the electrostatic lower hybrid drift instability. The predicted mode properties agree with observations. The waves are driven by the density gradient and the cross-field current associated with the **E** × **B** drifting electrons in the diffusion region. As V_E or $n_e^{-1}\partial n_e/\partial x$ decreases the growth rate decreases. The low V_E, and hence cross-field current, in the region where $T_\parallel/T_\perp$ peaks may explain why negligible lower hybrid wave activity is observed here, even though there is a density gradient. Similarly, the large $T_\parallel/T_\perp$ may also suppress the growth of the lower hybrid drift instability [*Huang et al.*, 2013].

In summary, the lower hybrid waves in the diffusion region are consistent with the electrostatic lower hybrid drift instability. The waves are driven at the density gradient in the presence of a large background electric field in the normal direction and propagate in the **E** × **B** direction. These waves are consistent with the lower hybrid drift waves reported in simulations of asymmetric reconnection [*Pritchett et al.*, 2012; *Pritchett*, 2013; *Roytershteyn et al.*, 2012].

2.5.2. Ion-Ion Cross-Field Instability

To model the instability near the ion edge, we consider a plasma with two unmagnetized ion populations and an electron population. We assume that the electrons are strongly magnetized and have zero drift. With these assumptions the electrostatic dispersion equation is

$$0 = 1 - \frac{\omega_{\rm pic}^2}{k^2 v_{\rm ic}} Z'\left(\frac{\omega - kV_{\rm ic}}{kv_{\rm ic}}\right) - \frac{\omega_{\rm pih}^2}{k^2 v_{\rm ih}^2} Z'\left(\frac{\omega - kV_{\rm ih}}{kv_{\rm ih}}\right) + \frac{\omega_{\rm pe}^2}{\Omega_{\rm ce}^2}\frac{1 - I_0(b)\exp(-b)}{b}, \qquad (5)$$

where the subscripts *ic* and *ih* refer to the cold and hot (magnetosheath crescent) ion populations, respectively. To solve equation (5), we assume $B = 50$ nT, $T_e = 100$ eV, $n_{ic} = 0.2$ cm^{-3}, $V_{ic} = 0$ and that V_{ih} is along the $-$**M** direction. In the magnetopause reference frame the cold ion velocity is small. We consider five cases which approximately model the changes in the ion distributions near the ion edge:

1. $T_{ic} = 20$ eV, $n_{ih} = 0.05$ cm^{-3}, $T_{ih} = 3000$ eV, $V_{ih} = 900$ km s^{-1}.
2. $T_{ic} = 30$ eV, $n_{ih} = 0.1$ cm^{-3}, $T_{ih} = 2500$ eV, $V_{ih} = 800$ km s^{-1}.
3. $T_{ic} = 40$ eV, $n_{ih} = 0.2$ cm^{-3}, $T_{ih} = 2000$ eV, $V_{ih} = 700$ km s^{-1}.
4. $T_{ic} = 60$ eV, $n_{ih} = 0.4$ cm^{-3}, $T_{ih} = 1700$ eV, $V_{ih} = 500$ km s^{-1}.
5. $T_{ic} = 80$ eV, $n_{ih} = 0.8$ cm^{-3}, $T_{ih} = 1500$ eV, $V_{ih} = 350$ km s^{-1}.

Case 1 corresponds to the distribution close to the ion edge, while case 5 corresponds to the distribution near the peak in the Larmor field.

The properties of the unstable modes predicted by equation (5) are presented in Figures 7d–7f, which show the dispersion relations, γ, and v_{ph}, respectively, as functions of k. Cases 1–4 all exhibit clear positive growth, while case 5 is marginally stable. This indicates that the instability is unstable when there is a large difference in bulk speeds between the ion populations perpendicular to **B** (as in Figure 6h). For case 5, V_{ih} is too small for significant wave growth and the mode is stabilized for smaller V_{ih} (closer to the magnetopause). Case 3, which corresponds to when the most intense waves are observed, has the largest growth rate. The wave number of the maximum growth rate is $k \approx 2.8 \times 10^{-4}$ m^{-1}, or equivalently $k\rho_e \approx 0.2$. This corresponds to $\lambda \approx 20$ km (similar wavelengths are predicted for cases 1, 2, and 4). These values of λ are less than a factor of two larger than the observed values (Table 1). However, there is some uncertainty in the observed λ because of possible changes in v_{ph} and f. In particular, we observe some differences between ϕ_B and ϕ_E over short time intervals in Figures 5f2–5i2, suggesting that v_{ph} may vary. The range of frequencies corresponding to γ_{max} is $0.4 \lesssim \omega/\omega_{LH} \lesssim 0.8$, comparable to observations in Figure 2g. As V_{ih} increases and n_{ih} decreases, ω/ω_{LH} and v_{ph} increase. Based on cases 1–4, the range of v_{ph} where γ is maximal is 300 km s^{-1} $\lesssim v_{ph} \lesssim$ 600 km s^{-1}, which agrees with the observations in Table 1. Therefore, the predicted mode properties are consistent with observations, so the ion-ion cross-field instability is the likely source of the waves near the ion edge.

These analyses suggest that the lower hybrid waves near the ion edge can only develop when there is a cold magnetospheric ion population. In the absence of cold ions (with only hot magnetospheric ions present) the ion-ion cross-field instability will not develop. Additionally, the instability requires ions propagating perpendicular to **B** as expected close to the X line [*Malakit et al.*, 2013; *Shay et al.*, 2016; *Phan et al.*, 2016]. Once generated the waves may contribute to the observed cold ion heating [*Toledo-Redondo et al.*, 2016]. Based on the estimated cold ion inflow speed 30–70 km s^{-1}, the cold ions can remain colocated with the waves for ~2–6 s, which is much longer than the inverse of the maximum growth rate of $2\pi\gamma^{-1} \approx 0.3$ s. This may explain the cold ion heating observed in Figure 6 before they are accelerated by the Larmor electric field. In contrast, the magnetosheath ions move much faster and undergo a partial gyroorbit before returning to the magnetosheath plasma, so they are likely less affected by the waves.

In summary, the lower hybrid waves near the ion edge are driven by the ion-ion cross-field instability, which develops because of the interaction between the cold magnetospheric ions and the crescent-shaped distribution of magnetosheath ions undergoing a partial gyroorbit into the magnetosphere. These waves are only likely to develop in the magnetospheric inflow region close to the X line when cold magnetospheric ions are present and are a possible source of cold ion heating. These waves have not been found in numerical simulations. Overall, the properties of the observed waves are consistent with predictions from electrostatic linear theory [*Papadopoulos et al.*, 1971; *Davidson and Gladd*, 1975; *Gary et al.*, 1987], which shows that different instabilities are responsible for the two groups of lower hybrid waves.

3. Discussion

The observed electron heating in the inflow region is consistent with electron trapping and heating by large-scale parallel electric fields, similar to previous observations [*Graham et al.*, 2014, 2016a]. The parallel accelerating potential $\Phi_{\|}$ associated with large-scale electric fields determines the degree of parallel electron heating in the magnetospheric inflow region [*Egedal et al.*, 2008, 2011]. Based on Figure 1h, it appears that the magnetosheath electrons, as well as the cold magnetospheric electrons, are heated; there is smooth change in the magnetosheath electron flux across the magnetopause to where the peak parallel heating is observed.

Therefore, there is a mixing of the magnetospheric and magnetosheath electrons close to the stagnation point where the parallel heating is observed. However, two-dimensional simulations suggest that the heated population is magnetospheric electrons, which are pulled into and trapped in the magnetospheric inflow region to neutralize the charge separation associated with magnetosheath ions undergoing finite gyroradius orbits in the magnetosphere [*Egedal et al.*, 2011; *Shay et al.*, 2016]. We can investigate which electron population is heated by comparing the density and temperature anisotropy with the background magnetospheric properties.

The observed anisotropy $T_{\|}/T_{\perp}<1$ of hot magnetospheric electrons throughout the inflow region indicates that the hot magnetospheric electrons are not trapped by $\Phi_{\|}$. Therefore, the parallel potential $\Phi_{\|}$ should satisfy $\Phi_{\|}<2$ keV but be sufficiently large to trap and accelerate the cold magnetospheric electrons or magnetosheath electrons, such that the temperature anisotropy reaches $T_{\|c}/T_{\perp c}=5.5$. By using the fitting routine in *Graham et al.* [2016a] we estimate the maximum $\Phi_{\|}$ to be $\approx$ 600 V, about a factor of 3 larger than previous observations [*Graham et al.*, 2014, 2016a]. Based on the fit, we estimate $T_{\perp} \approx 100$ eV (using a Maxwellian fit to the distribution at $\theta = 90°$) when $\Phi_{\|}$ peaks. For the observed electron distribution when $T_{\|c}/T_{\perp c}$ peaks, the predicted upstream density required to model the observed distribution is $n_{e\infty} \approx [0.4-1.5]$ cm^{-3}, which is larger than the magnetospheric density $n_e=0.2$ cm^{-3}. This discrepancy suggests that the heated electron distribution contains magnetosheath electrons, which have crossed the magnetopause boundary. Moreover, closer to the magnetopause boundary $T_{\|}>T_{\perp}$ remains while the density increases, which corresponds to the increased density of magnetosheath electrons. Here the electron distribution is composed primarily of magnetosheath electrons. Qualitatively, the changes in the electron differential energy fluxes (Figure 1f) are consistent with the sheath electrons crossing the magnetopause, mixing with the cold magnetospheric electrons, and being heated; there is a continuous evolution in the magnetosheath fluxes to higher energies across the magnetopause.

Based on the scaling equations in *Egedal et al.* [2013], $\Phi_{\|}$ is related to the upstream conditions by $\Phi_{\|}= \pi T_{e\infty} n_e^2 B_{\infty}^2 / \left(4 n_{e\infty}^2 B^2\right)$, where the ∞ subscripts denote the upstream parameters. Assuming the upstream parameters are the conditions in the magnetosphere we calculate $\Phi_{\|}=1800$ V where $T_{\|c}/T_{\perp c}$ peaks, which is significantly larger than the $\Phi_{\|}$ estimated from the observed distributions. Similarly, we can calculate the predicted $T_{\|}/T_{\perp}$ using $T_{\|}/T_{\perp} = \pi n_e^2 B_{\infty}^3 / \left(6 n_{\infty}^3 B^3\right)$. Assuming the upstream conditions are magnetospheric, we estimate $T_{\|}/T_{\perp} \sim 40$ where $T_{\|c}/T_{\perp c}$ peaks, which is much larger than the observed peaks in $T_{\|c}/T_{\perp c}$. We conclude that the parallel electron heating cannot be explained by trapping of the cold magnetospheric electron population alone. The observed $T_{\|c}/T_{\perp c}$ can only be explained by a plasma of predominantly magnetosheath electrons crossing the magnetopause and being trapped in the magnetospheric inflow region. This raises the question of how magnetosheath electrons are able to cross the magnetopause boundary. One explanation is the presence of the large-amplitude lower hybrid waves observed in the diffusion region and magnetospheric separatrices, enabling the electrons to cross the magnetopause, for instance, by cross-field diffusion.

We now consider whether the lower hybrid waves can enable magnetosheath electrons to cross the magnetopause boundary and their contributions to the anomalous terms in Ohm's law. Using the four spacecraft, we can estimate the terms associated with anomalous drag, anomalous momentum transport in the **M** direction, and the cross-field diffusion in the **N** direction. The anomalous drag is defined as $\mathbf{D}=-\langle \delta n_e \delta \mathbf{E} \rangle / \langle n_e \rangle$ and $T_M=\langle \delta V_{eN} \delta B_L \rangle$ is associated with anomalous momentum transport. To compute the cross-field diffusion coefficient, we use $D_{\perp}=\delta n_e \delta V_{eN}/\nabla n_e$ [*Vaivads et al.*, 2004]. Here δ indicates the fluctuating terms ($f>10$ Hz), and $\langle \dots \rangle$ indicates spatial averaging. Ideally, the quantities would be averaged over the **M** direction (as is done in three-dimensional simulations); however, here we average over the four spacecraft, then low-pass filter below 10 Hz to remove fluctuations at the lower hybrid frequency. For this event the FPI electron density and velocity moments cannot resolve lower hybrid fluctuations so we estimate δn_e using the fluctuations in the spacecraft potentials and calculate $\delta \mathbf{V}_e$ using $\delta \mathbf{V}_e = \delta \mathbf{E} \times \mathbf{B}/|\mathbf{B}|^2$ (the component of $\delta \mathbf{V}_e$ parallel to **B** is therefore neglected).

The results are shown in Figure 8. Figures 8b and 8c show that the largest δn_e are associated with the lower hybrid waves in the diffusion region. Near the ion edge δn_e is relatively small, but n_e is also small. Figure 8d shows that **D** peaks when the two groups of lower hybrid waves are observed, with maximum values of $\sim$0.5 mV m^{-1}. The maximum value of T_M (Figure 8e) associated with ion diffusion region is about an order of magnitude smaller than **D**. For the ion edge lower hybrid waves T_M is negligible because $\delta \mathbf{B}$ is small for these waves (Figure 2h). This suggests that T_M has negligible effect on the reconnection electric field. In the **N**

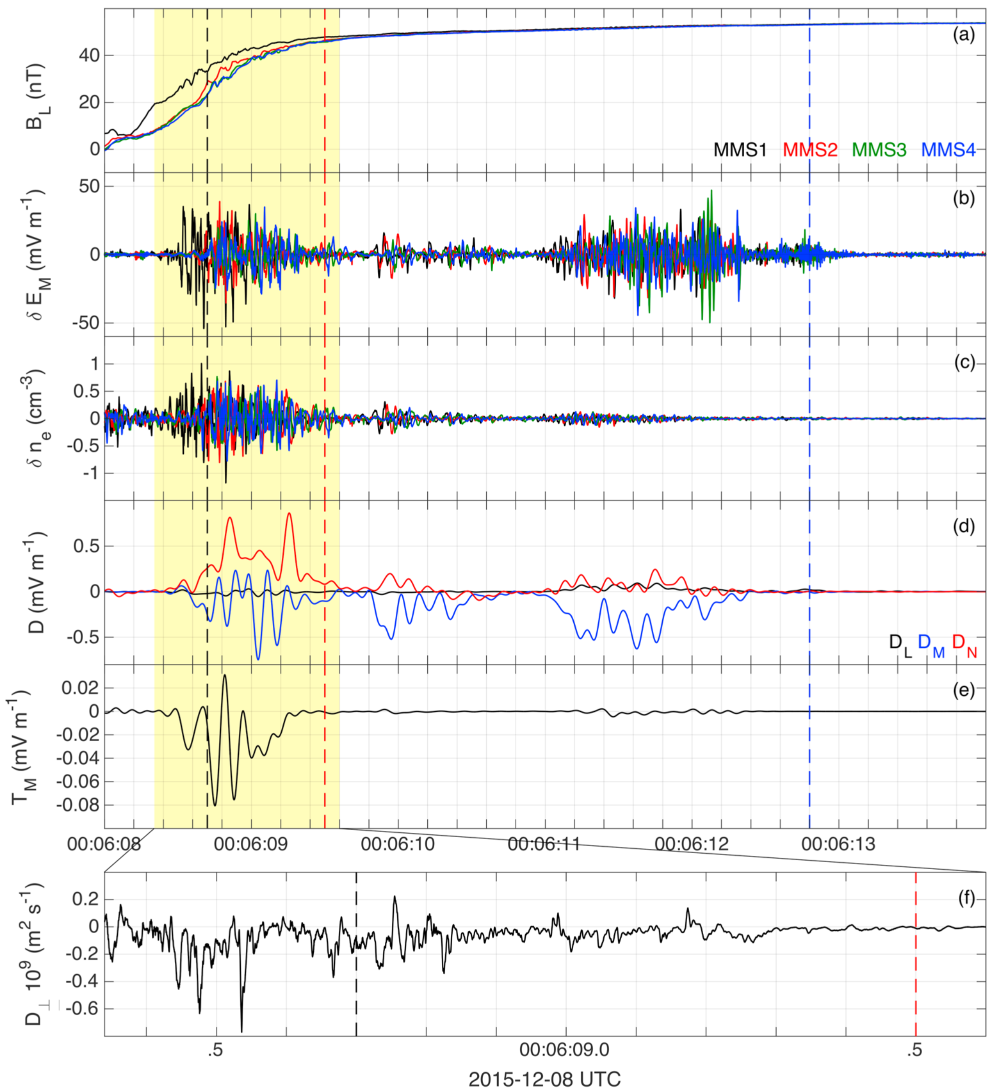

Figure 8. Anomalous terms associated with the lower hybrid waves in the ion diffusion region and magnetospheric inflow region.(a) B_L obtained from MMS1–MMS4. (b) δE_M. (c) δn_e. (d and e) Anomalous drag **D** and anomalous transport T_M in the **M** direction estimated over the four spacecraft. (f) Cross-field diffusion coefficient $D_\perp$ associated with the diffusion region lower hybrid waves averaged over the four spacecraft. The black, red, and blue dashed lines mark the diffusion region, peak parallel electron heating, and ion edge, respectively.

direction the magnitude of **D** is well below the magnitude of the Hall term but could be comparable to the pressure term in equation (1). In the **M** direction the four-spacecraft averaged **E** and $\mathbf{E}+\mathbf{V}_i\times\mathbf{B}$ are much smaller than in the **N** direction but are still large compared with D_M and T_M. The peak values of **D** and T_M become significantly larger without low-pass filtering but fluctuate more. These fluctuations are not likely to correspond to anomalous fields. Overall, our results are consistent with previous observations and simulations of anomalous drag associated with asymmetric reconnection [*Mozer et al.*, 2011; *Pritchett*, 2013] but are smaller than the values obtained by *Price et al.* [2016].

The cross-field diffusion coefficient $D_\perp$ averaged over the four spacecraft is shown in Figure 8f for the lower hybrid waves in the ion diffusion region. Throughout this region $D_\perp$ is generally negative, corresponding to particle diffusion from the magnetosheath to the magnetosphere. The magnitude of $D_\perp$ peaks at $\sim -0.8 \times 10^9$ m^2 s^{-1}, consistent with previous estimates [*Vaivads et al.*, 2004] and theoretical predictions [*Treumann et al.*, 1991]. These lower hybrid waves may then enable magnetosheath electrons to enter the magnetospheric inflow, where they are heated and accelerated parallel to **B**. The lower hybrid waves and associated particle diffusion may broaden the density gradient [*Khotyaintsev et al.*, 2016], such that the electron pressure term in equation (1) remains relatively small compared with the Hall term (Figure 3d).

4. Conclusions

In this paper we investigate the properties of the lower hybrid waves in the ion diffusion region and magnetospheric inflow region of asymmetric magnetic reconnection using data from the MMS spacecraft. The reconnection event is approximately antiparallel (negligible guide field) and is highly asymmetric. Cold magnetospheric ions and electrons are observed in the magnetospheric plasma. The key results of this study are as follows:

1. The ion diffusion region and magnetospheric inflow region are highly structured for asymmetric reconnection, with a number of distinct boundaries observed. In particular, two distinct groups of large-amplitude lower hybrid waves are observed within one ion gyroradius of the magnetopause boundary. These two groups of waves are observed in the ion diffusion region and near the ion edge. The waves have similar wavelengths but propagate in opposite directions along the magnetopause at different phase speeds. The region of intense parallel electron heating is located between two groups of lower hybrid waves. The peak parallel heating occurs near the stagnation point where negligible wave activity is observed.
2. Near the ion edge, the lower hybrid waves are driven by the ion-ion cross-field instability. This instability develops from the interaction between cold magnetospheric ions and magnetosheath ions entering the magnetosphere through the finite gyroradius effect. These waves provide a source of heating for the cold magnetospheric ions. The waves propagate in the direction of the crescent-shaped distribution of magnetosheath ions (duskward).
3. In the diffusion region the lower hybrid waves are driven by the lower hybrid drift instability at the density gradient and propagate in the local $\mathbf{E} \times \mathbf{B}$ direction (dawnward). These waves provide a possible source of cross-field diffusion from the magnetosheath to the magnetosphere, allowing magnetosheath electrons to enter the magnetospheric inflow region, which can broaden the density gradient between the magnetospheric and magnetosheath plasmas.

Acknowledgments
We thank the entire MMS team and instrument PIs for data access and support. We thank the SCM team for the high-quality magnetic field data. This work was supported by the Swedish National Space Board, grant 175/15. MMS data are available at https://lasp.colorado.edu/mms/sdc/public.

References

André, M., and C. M. Cully (2012), Low-energy ions: A previously hidden solar system particle population, *Geophys. Res. Lett.*, *39*, L03101, doi:10.1029/2011GL050242.

Bale, S. D., F. S. Mozer, and T. Phan (2002), Observation of lower hybrid drift instability in the diffusion region at a reconnecting magnetopause, *Geophys. Res. Lett.*, *29*(24), 2180, doi:10.1029/2002GL016113.

Burch, J. L., T. E. Moore, R. B. Torbert, and B. L. Giles (2016), Magnetospheric multiscale overview and science objectives, *Space Sci. Rev.*, *199*, 5–21, doi:10.1007/s11214-015-0164-9.

Cairns, I. H., and B. F. McMillan (2005), Electron acceleration by lower hybrid waves in magnetic reconnection regions, *Phys. Plasmas*, *12*, 102110, doi:10.1063/1.2080567.

Cassak, P. A., and M. A. Shay (2007), Scaling of asymmetric magnetic reconnection: General theory and collisional simulations, *Phys. Plasmas*, *14*, 102114, doi:10.1063/1.2795630.

Chandler, M. O., S. A. Fuselier, M. Lockwood, and T. E. Moore (1999), Evidence of component merging equatorward of the cusp, *J. Geophys. Res.*, *104*, 22,623–22,634, doi:10.1029/1999JA900175.

Daughton, W. (2003), Electromagnetic properties of the lower-hybrid drift instability in a thin current sheet, *Phys. Plasmas*, *10*, 3103–3119, doi:10.1063/1.1594724.

Davidson, R. C., and N. T. Gladd (1975), Anomalous transport properties associated with the lower-hybrid-drift instability, *Phys. Fluids*, *18*, 1327–1335, doi:10.1063/1.861021.

Dunlop, M. W., D. J. Southwood, K.-H. Glassmeier, and F. M. Neubauer (1988), Analysis of multipoint magnetometer data, *Adv. Space Res.*, *8*, 273–277, doi:10.1016/0273-1177(88)90141-X.

Egedal, J., W. Fox, N. Katz, M. Porkolab, M. Oieroset, R. P. Lin, W. Daughton, and J. F. Drake (2008), Evidence and theory for trapped electrons in guide field magnetotail reconnection, *J. Geophys. Res.*, *113*, A12207, doi:10.1029/2008JA013520.

Egedal, J., A. Le, P. L. Pritchett, and W. Daughton (2011), Electron dynamics in two-dimensional asymmetric anti-parallel reconnection, *Phys. Plasmas*, *18*, 102901, doi:10.1063/1.3646316.

Egedal, J., A. Le, and W. Daughton (2013), A review of pressure anisotropy caused by electron trapping in collisionless plasma, and its implications for magnetic reconnection, *Phys. Plasmas*, *20*, 061201, doi:10.1063/1.4811092.

Ergun, R. E., et al. (2016), The axial double probe and fields signal processing for the MMS mission, *Space Sci. Rev.*, *199*, 167–188, doi:10.1007/s11214-014-0115-x.

Gary, S. P., R. L. Tokar, and D. Winke (1987), Ion/ion and electron/ion cross-field instabilities near the lower hybrid frequency, *J. Geophys. Res.*, *92*, 10,029–10,038, doi:10.1029/JA092iA09p10029.

Graham, D. B., Y. V. Khotyaintsev, A. Vaivads, M. André, and A. N. Fazakerley (2014), Electron dynamics in the diffusion region of an asymmetric magnetic reconnection, *Phys. Rev. Lett.*, *112*, 215004, doi:10.1103/PhysRevLett.112.215004.

Graham, D. B., et al. (2016a), Electron currents and heating in the ion diffusion region of asymmetric reconnection, *Geophys. Res. Lett.*, *43*, 4691–4700, doi:10.1002/2016GL068613.

Graham, D. B., A. Vaivads, Y. V. Khotyaintsev, and M. André (2016b), Whistler emission in the separatrix regions of asymmetric reconnection, *J. Geophys. Res. Space Physics*, *121*, 1934–1954, doi:10.1002/2015JA021239.

Henderson, P. D., C. J. Owen, A. D. Lahiff, I. V. Alexeev, A. N. Fazakerley, E. Lucek, and H. Rème (2006), Cluster PEACE observations of electron pressure tensor divergence in the magnetotail, *Geophys. Res. Lett.*, *33*, L22106, doi:10.1029/2006GL027868.

Huang, F., G. Liu, Y. Chen, M. Y. Yu, F. Yan, Y. Deng, and H. Chen (2013), Lower hybrid drift instability in a current sheet with anisotropic temperature, *Phys. Scr.*, *87*, 065501, doi:10.1088/0031-8949/87/06/065501.

Innocenti, M. E., C. Norgren, D. Newman, M. Goldman, S. Markidis, and G. Lapenta (2016), Study of electric and magnetic field fluctuations from lower hybrid drift instability waves in the terrestrial magnetotail with the fully kinetic, semi-implicit, adaptive multi level multi domain method, *Phys. Plasmas*, *23*, 052902, doi:10.1063/1.4952630.

Khotyaintsev, Y. V., A. Vaivads, A. Retinò, M. André, C. J. Owen, and H. Nilsson (2006), Formation of inner structure of a reconnection separatrix region, *Phys. Rev. Lett.*, *97*, 205003, doi:10.1103/PhysRevLett.97.205003.

Khotyaintsev, Y. V., et al. (2016), Electron jet of asymmetric reconnection, *Geophys. Res. Lett.*, *43*, 5571–5580, doi:10.1002/2016GL069064.

Krall, N. A., and P. C. Liewer (1971), Low-frequency instabilities in magnetic pulses, *Phys. Rev. A*, *4*, 2094, doi:10.1103/PhysRevA.4.2094.

Lavraud, B., et al. (2016), Currents and associated electron scattering and bouncing near the diffusion region at Earth's magnetopause, *Geophys. Res. Lett.*, *43*, 3042–3050, doi:10.1002/2016GL068359.

Le Contel, O., et al. (2016), The search-coil magnetometer for MMS, *Space Sci. Rev.*, *199*, 257–282, doi:10.1007/s11214-014-0096-9.

Lindqvist, P.-A., et al. (2016), The spin-plane double probe electric field instrument for MMS, *Space Sci. Rev.*, *199*, 137–165, doi:10.1007/s11214-014-0116-9.

Malakit, K., M. A. Shay, P. A. Cassak, and D. Ruffolo (2013), New electric field in asymmetric magnetic reconnection, *Phys. Rev. Lett.*, *111*, 135001, doi:10.1103/PhysRevLett.111.135001.

Mozer, F. S., V. Angelopoulos, J. Bonnell, K. H. Glassmeier, and J. P. McFadden (2008), THEMIS observations of modified Hall fields in asymmetric magnetic field reconnection, *Geophys. Res. Lett.*, *35*, L17S04, doi:10.1029/2007GL033033.

Mozer, F. S., M. Wilber, and J. F. Drake (2011), Wave associated anomalous drag during magnetic field reconnection, *Phys. Plasmas*, *18*, 102902, doi:10.1063/1.3647508.

Norgren, C., A. Vaivads, Y. V. Khotyaintsev, and M. Andre (2012), Lower hybrid drift waves: Space observations, *Phys. Rev. Lett.*, *109*, 055001, doi:10.1103/PhysRevLett.109.055001.

Papadopoulos, K., R. C. Davidson, J. M. Dawson, I. Haber, D. A. Hammer, N. A. Krall, and R. Shanny (1971), Heating of counterstreaming ion beams in an external magnetic field, *Phys. Fluids*, *14*, 849–857, doi:10.1063/1.1693520.

Paschmann, G., I. Papamastorakis, N. Sckopke, G. Haerendel, B. U. O. Sonnerup, S. J. Bame, J. R. Asbridge, J. T. Gosling, C. T. Russel, and R. C. Elphic (1979), Plasma acceleration at the Earth's magnetopause—Evidence for reconnection, *Nature*, *282*, 243–246, doi:10.1038/282243a02.

Phan, T. D., et al. (2016), Ion larmor radius effects near a reconnection X line at the magnetopause: THEMIS observations and simulation comparison, *Geophys. Res. Lett.*, *43*, 8844–8852, doi:10.1002/2016GL070224.

Pollock, C., et al. (2016), Fast plasma investigation for magnetospheric multiscale, *Space Sci. Rev.*, *199*, 331–406, doi:10.1007/s11214-016-0245-4.

Price, L., M. Swisdak, J. F. Drake, P. A. Cassak, J. T. Dahlin, and R. E. Ergun (2016), The effects of turbulence on three-dimensional magnetic reconnection at the magnetopause, *Geophys. Res. Lett.*, *43*, 6020–6027, doi:10.1002/2016GL069578.

Priest, E. R., and T. Forbes (2000), *Magnetic Reconnection: MHD Theory and Applications*, Cambridge Univ. Press, Cambridge, U. K.

Pritchett, P. L. (2008), Collisionless magnetic reconnection in an asymmetric current sheet, *J. Geophys. Res.*, *113*, A06210, doi:10.1029/2007JA012930.

Pritchett, P. L. (2013), The influence of intense electric fields on three-dimensional asymmetric magnetic reconnection, *Phys. Plasmas*, *20*, 061204, doi:10.1063/1.4811123.

Pritchett, P. L., F. S. Mozer, and M. Wilber (2012), Intense perpendicular electric fields associated with three-dimensional magnetic reconnection at the subsolar magnetopause, *J. Geophys. Res.*, *117*, A06212, doi:10.1029/2012JA017533.

Roytershteyn, V., W. Daughton, H. Karimabadi, and F. S. Mozer (2012), Influence of the lower-hybrid drift instability on magnetic reconnection in asymmetric configurations, *Phys. Rev. Lett.*, *108*, 185001, doi:10.1103/PhysRevLett.108.185001.

Russell, C. T., et al. (2016), The magnetospheric multiscale magnetometers, *Space Sci. Rev.*, *199*, 189–256, doi:10.1007/s11214-014-0057-3.

Sauvaud, J.-A., et al. (2001), Intermittent thermal plasma acceleration linked to sporadic motions of the magnetopause, first Cluster results, *Ann. Geophys.*, *19*, 1523–1532, doi:10.5194/angeo-19-1523-2001.

Shay, M. A., T. D. Phan, C. C. Haggerty, M. Fujimoto, J. F. Drake, K. Malakit, P. A. Cassak, and M. Swisdak (2016), Kinetic signatures of the region surrounding the X line in asymmetric (magnetopause) reconnection, *Geophys. Res. Lett.*, *43*, 4145–4154, doi:10.1002/2016GL069034.

Silin, I., J. Buchner, and A. Vaivads (2005), Anomalous resistivity due to nonlinear lower-hybrid drift waves, *Phys. Plasmas*, *12*, 062902, doi:10.1063/1.1927096.

Sonnerup, B. U. O., G. Paschmann, I. Papamastorakis, N. Sckopke, G. Haerendel, S. J. Bame, J. R. Asbridge, J. T. Gosling, and C. T. Russell (1981), Evidence for magnetic field reconnection at the Earth's magnetopause, *J. Geophys. Res.*, *86*, 10,049–10,067.

Swisdak, M., B. N. Rogers, J. F. Drake, and M. A. Shay (2003), Diamagnetic suppression of component magnetic reconnection at the magnetopause, *J. Geophys. Res.*, *108*(A5), 1218, doi:10.1029/2002JA009726.

Toledo-Redondo, S., M. André, A. Vaivads, Y. V. Khotyaintsev, B. Lavraud, D. B. Graham, A. Divin, and N. Aunai (2016), Cold ion heating at the dayside magnetopause during magnetic reconnection, *Geophys. Res. Lett.*, *43*, 58–66, doi:10.1002/2015GL067187.

Treumann, R. A., J. Labelle, and R. Pottelette (1991), Plasma diffusion at the magnetopause—The case of lower hybrid drift waves, *J. Geophys. Res.*, *96*, 16,009–16,013, doi:10.1029/91JA01671.

Vaivads, A., M. André, S. C. Buchert, J.-E. Wahlund, A. N. Fazakerley, and N. Cornilleau-Wehrlin (2004), Cluster observations of lower hybrid turbulence within thin layers at the magnetopause, *Geophys. Res. Lett.*, *31*, L03804, doi:10.1029/2003GL018142.

Wang, R., Q. Lu, C. Huang, and S. Wang (2010), Multispacecraft observation of electron pitch angle distributions in magnetotail reconnection, *J. Geophys. Res.*, *115*, A01209, doi:10.1029/2009JA014553.

Wang, S., et al. (2016), Two-scale ion meandering caused by the polarization electric field during asymmetric reconnection, *Geophys. Res. Lett.*, *43*, 7831–7839, doi:10.1002/2016GL069842.